

## DIRECT IMAGING BY *SDO* AIA OF QUASI-PERIODIC FAST PROPAGATING WAVES OF $\sim 2000$ km s<sup>-1</sup> IN THE LOW SOLAR CORONA

WEI LIU<sup>1,2</sup>, ALAN M. TITLE<sup>1</sup>, JUNWEI ZHAO<sup>2</sup>, LEON OFMAN<sup>3</sup>, CAROLUS J. SCHRIJVER<sup>1</sup>, MARKUS J. ASCHWANDEN<sup>1</sup>, BART DE PONTIEU<sup>1</sup>, AND THEODORE D. TARBELL<sup>1</sup>

*Accepted by ApJ Letters, June 13, 2011*

### ABSTRACT

Quasi-periodic, propagating fast mode magnetosonic waves in the corona were difficult to observe in the past due to relatively low instrument cadences. We report here evidence of such waves directly imaged in EUV by the new *SDO* AIA instrument. In the 2010 August 1 C3.2 flare/CME event, we find arc-shaped wave trains of 1–5% intensity variations (lifetime  $\sim 200$  s) that emanate near the flare kernel and propagate outward up to  $\sim 400$  Mm along a funnel of coronal loops. Sinusoidal fits to a typical wave train indicate a phase velocity of  $2200 \pm 130$  km s<sup>-1</sup>. Similar waves propagating in opposite directions are observed in closed loops between two flare ribbons. In the  $k$ – $\omega$  diagram of the Fourier wave power, we find a bright ridge that represents the dispersion relation and can be well fitted with a straight line passing through the origin. This  $k$ – $\omega$  ridge shows a broad frequency distribution with indicative power at 5.5, 14.5, and 25.1 mHz. The strongest signal at 5.5 mHz (period 181 s) temporally coincides with quasi-periodic pulsations of the flare, suggesting a common origin. The instantaneous wave energy flux of  $(0.1\text{--}2.6) \times 10^7$  ergs cm<sup>-2</sup> s<sup>-1</sup> estimated at the coronal base is comparable to the steady-state heating requirement of active region loops.

*Subject headings:* Sun: activity—Sun: corona—Sun: coronal mass ejections—Sun: flares—Sun: oscillations—waves

### 1. INTRODUCTION

In the last decade, observations from *SOHO*, *TRACE*, *Hinode*, and ground-based instruments have led to detection of various modes of magnetohydrodynamic (MHD) waves in the solar corona (see review by Nakariakov & Verwichte 2005), including (1) oscillations or standing waves of slow modes (Wang et al. 2002; Ofman & Wang 2002), fast kink modes (periods: 2–10 min; Aschwanden et al. 1999; Schrijver et al. 1999), and fast sausage modes (periods: 1–60 s; Nakariakov et al. 2003), and (2) propagating waves of slow modes (Ofman et al. 1997; Deforest & Gurman 1998; De Moortel et al. 2000; Ofman & Wang 2008) and Alfvén waves (Tomczyk et al. 2007; De Pontieu et al. 2007; Cirtain et al. 2007; Okamoto et al. 2007; Jess et al. 2009; Liu et al. 2009; some of which were interpreted as kink waves, see Van Doorselaere et al. 2008).

Quasi-periodic propagating fast mode magnetosonic waves with phase speeds  $v_{\text{ph}} \sim 1000$  km s<sup>-1</sup> in active regions remain the least observed among all coronal MHD waves, while single-pulse “EIT waves” (Thompson et al. 1998) of typical speeds  $\sim 200$  km s<sup>-1</sup> were interpreted as their quiet Sun counterparts (Wu et al. 2001; Ofman & Thompson 2002; cf., Chen & Wu 2011). Williams et al. (2002) first imaged during an eclipse a fast wave of  $v_{\text{ph}} = 2100$  km s<sup>-1</sup> in a closed loop. Verwichte et al. (2005) later observed with *TRACE* fast kink modes of  $v_{\text{ph}} = 200\text{--}700$  km s<sup>-1</sup> in an open-field

supra-arcade.

The scarcity of fast wave observations was mainly due to instrumental limitations. The new Atmospheric Imaging Assembly (AIA; Lemen et al. 2011) on the *Solar Dynamics Observatory* (*SDO*) has high cadences up to 10 s, short exposures of 0.1–2 s, and a  $41' \times 41'$  full-Sun field of view (FOV) at  $1''.5$  resolution, which are all crucial for detecting fast propagating features. Within the first year of its launch, AIA has detected 10 quasi-periodic fast propagating (QFP) waves, among which the first was mentioned by Liu et al. (2010b) and the best example is presented here.

### 2. OBSERVATIONS AND DATA ANALYSIS

On 2010 August 1, an eruption (Liu et al. 2010a; Schrijver & Title 2011) occurred in NOAA active region 11092, involving a coronal mass ejection (CME) and a *GOES* C3.2 flare that started at 07:25 UT and peaked at 08:57 UT.

#### 2.1. Space-time Analysis

##### 2.1.1. Waves in the Funnel

In AIA 171 Å running difference images (Figure 1(d)–(f), Animation 1(D)) and even direct and base difference images (Animations 1(A) and 1(C)), we discovered arc-shaped wave trains emanating near the brightest flare kernel (box 1 in Figure 1(b)) and rapidly propagating outward along a funnel of coronal loops that subtend an angle of  $\sim 60^\circ$  near the corona base. They are successive, alternating intensity variations of 1–5%, repeatedly launched in the wake of the CME during the rise phase of the flare (07:45–08:45 UT). The wave fronts continuously travel beyond the limb, suggesting that they are not propagating over the solar surface like Moreton (1960) or EIT waves. They are not observed in the other AIA EUV channels, indicating subtle temperature dependence.

<sup>1</sup> Lockheed Martin Solar and Astrophysics Laboratory, Building 252, 3251 Hanover Street, Palo Alto, CA 94304

<sup>2</sup> W. W. Hansen Experimental Physics Laboratory, Stanford University, Stanford, CA 94305

<sup>3</sup> Catholic University of America and NASA Goddard Space Flight Center, Code 671, 8800 Greenbelt Road, Greenbelt, MD 20771, USA

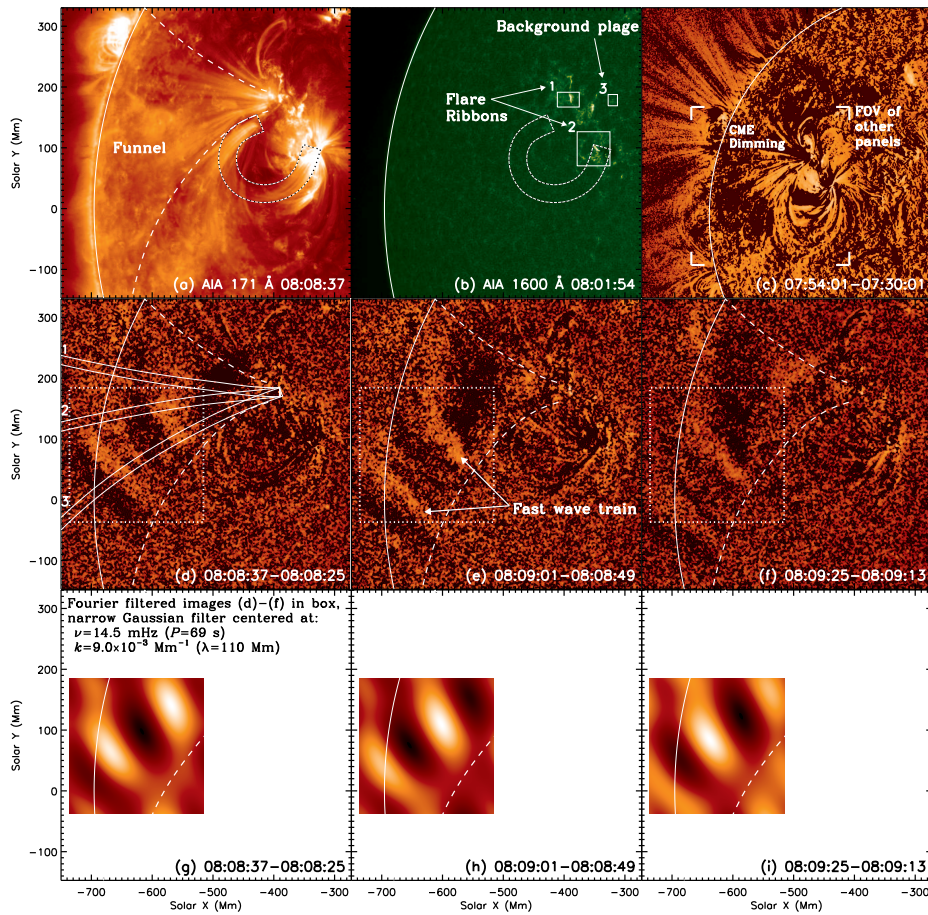


FIG. 1.— SDO AIA images of QFP waves. (a) 171 Å image (see Animation 1(A)) showing the funnel and loop in which fast waves propagate. (b) 1600 Å image (Animation 1(B)) showing flare ribbons. (c) 171 Å base difference image (Animation 1(C)) showing dimming behind the CME front. The four brackets mark the smaller FOV of the other panels. (d)–(f) 171 Å running difference images (Animation 1(D)) showing successive wave fronts propagating in the funnel. The three curved cuts are used to obtain space-time diagrams shown in Figure 2. The square box marks the region for Fourier analysis in Section 2.2. (g)–(i) Images of (d)–(f) in the boxed region Fourier filtered with a narrow Gaussian centered at the peak in Figure 4(b) at frequency  $\nu = 14.5$  mHz ( $P = 69$  s) and wave number  $k = 9.0 \times 10^{-3}$  Mm $^{-1}$  ( $\lambda = 110$  Mm), which highlight the corresponding QFP wave trains (see Animation 1(E) and Section 2.2.3).

To analyze wave kinematics, we placed three 20'' (14.7 Mm) wide curved cuts that start from the brightest flare kernel and follow the shape of the funnel (Figure 1(d)). By averaging pixels across each cut, we obtained image profiles along it and stacking these profiles over time gives space-time diagrams as shown in Figure 2, where we see two types of moving features:

(1) The shallow, gradually accelerating stripes represent the expanding coronal loops in the CME that have final velocities up to  $\geq 260$  km s $^{-1}$  as indicated by parabolic fits (dashed lines in Figure 2(b)). EUV dimming is evident behind these loops (Figures 1(c) and 2(d)), indicating evacuation of coronal mass.

(2) The steep, recurrent stripes result from the arch-shaped wave fronts. Sinusoidal fits (Figure 2(e)) to the spatial profiles along the central cut yield a projected wavelength  $\lambda = 133 \pm 17$  Mm and phase velocity  $v_{\text{ph}} = 2200 \pm 130$  km s $^{-1}$ , giving a period of  $P = \lambda/v_{\text{ph}} = 60 \pm 8$  s. Linear fits to the space-time stripes from the three cuts produced by the same wave front indicate similar velocities (Figure 2(a)–(c)). (Such velocities measured from projection on the sky plane are lower limits of their 3D values.) Each wave front travels up to  $\sim 400$  Mm with a lifetime of  $\sim 200$  s before reaching the edge of AIA’s

FOV, likely resulting from damping and amplitude decay with distance ( $\propto 1/r^2$ ).

### 2.1.2. Waves in Closed Loops

At the same time, we noticed similar fast propagating waves along closed loops between two flare ribbons (Figures 1(a) and (b)). The space-time diagram (Figure 3(a)) from the loop-shaped cut reveals steep stripes of both positive and negative slopes, particularly near the two footpoints, which represent waves propagating in opposite directions. The bi-directional propagation can be evidently seen separately in Fourier filtered space-time diagrams (Figures 3(b) and (c); see Tomczyk & McIntosh 2009). The linearly fitted phase velocities are similar in the two directions (1000–2000 km s $^{-1}$ ). The sudden switches of direction at the western footpoint (top edge of the plot) near 08:10 and 08:25 UT suggest wave reflection, but a general trend cannot be established. It is thus not clear whether the bi-directional waves are generated independently, or they are the same wave trains reflected repeatedly between the footpoints,

We find no temporal correlation between the waves in the closed loops and those in the funnel that is dominated by outgoing waves, except for marginal incoming wave



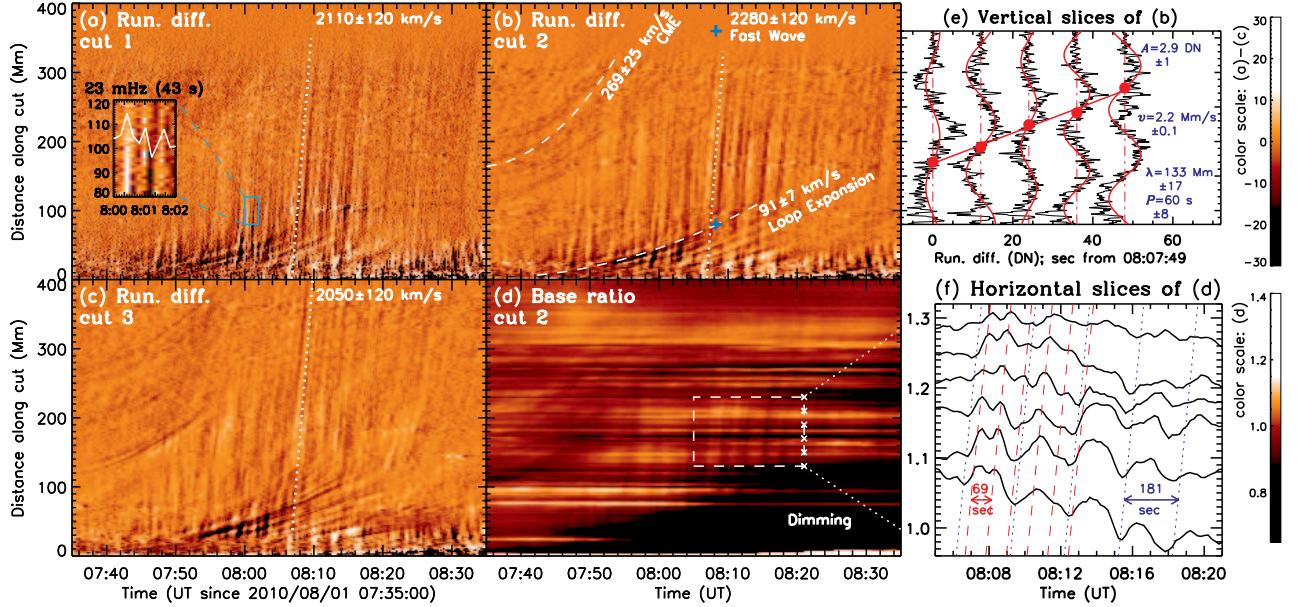


FIG. 2.— Space-time analysis of waves in the funnel. (a)–(c) Running difference space-time diagrams obtained from AIA 171 Å images along the three cuts shown in Figure 1(d). The insert in (a) offers an enlarged view for the selected region, overlaid with a distance averaged profile showing a 43 s periodicity. (d) Base ratio space-time diagram of cut 2 obtained by normalizing image profiles with a pre-event profile. All the space-time diagrams are smoothed with a  $3 \times 3$  pixel boxcar, except for (a) which is smoothed in space only. (e) Vertical slices of (b) at times and distances marked by the two plus signs. They are snapshots of intensity running difference (x-axis) as a function of distance (y-axis) at five consecutive times. Each curve (and thus its average position, marked by the vertical broken line) is incrementally shifted by 12 DN which equals AIA’s 12 s cadence and thus the x-axis also serves as elapsed time. Each profile is fitted with a sine function  $A \sin[2\pi(r - r_0)/\lambda]$  shown in red, where  $A$  is the amplitude,  $\lambda$  wavelength, and  $r_0$  the initial phase in distance. The average fitted parameters and their standard deviations are listed. The filled circles mark the delayed occurrences at the average position, to which a linear fit indicates a phase velocity  $v_{\text{ph}} = 2200 \pm 130 \text{ km s}^{-1}$ . (f) Horizontal slices of (d) in the selected region, i.e., temporal profiles of intensity base ratio at locations marked by the cross signs. Successive curves at greater distances are shifted upward. The two prominent wave periods of 69 and 181 s are marked with slanted lines, indicating wave propagation.

signals near its base (Figure 2). Because of their simplicity (no superposition of bi-directional propagation), we choose to further analyze the waves in the funnel with Fourier transform as presented below.

## 2.2. Fourier Analysis of Waves in the Funnel

### 2.2.1. Overall $k$ - $\omega$ Diagram

We extracted a 3D data cube in  $(x, y, t)$  coordinates, i.e., a time series of 171 Å running difference images for the FOV of Figure 1(a) during 07:45–08:45 UT. We obtained the Fourier power of the data cube on the  $(k_x, k_y, \nu)$  basis of wave number  $k_x$  and  $k_y$  and frequency  $\nu$ . We then summed the power in the azimuthal  $\theta$  direction of cylindrical coordinates  $(k, \theta, \nu)$ , where  $k = \sqrt{k_x^2 + k_y^2}$  (e.g., DeForest 2004). This yields a  $k$ - $\omega$  diagram of wave power at a resolution of  $\Delta k = 2.09 \times 10^{-3} \text{ Mm}^{-1}$  and  $\Delta \nu = 0.277 \text{ mHz}$  as shown in Figure 4(a). We find a steep, narrow ridge that describes the dispersion relation of the fast propagating waves, together with a shallow, diffuse ridge that represents those slowly expanding loops at velocities on the order of  $50 \text{ km s}^{-1}$ .

To isolate the fast propagating waves (at the expense of reduced frequency resolution), we repeated this analysis for a smaller boxed region as shown in Figure 1(d) and a shorter duration of 07:58–08:23 UT in which these waves are prominent. The resulting  $k$ - $\omega$  diagram (Figure 4b) better shows the steep ridge that can be fitted with a straight line passing through the origin. This gives average phase ( $v_{\text{ph}} = \nu/k$ ) and group ( $v_{\text{gr}} = d\nu/dk$ ) veloci-

ties of  $1630 \pm 760 \text{ km s}^{-1}$ , which cannot be distinguished in the observed range up to the Nyquist frequency of 41.7 mHz given by AIA’s 12 s cadence due to the large uncertainty.

### 2.2.2. Temporal Evolution of $k$ - $\omega$ Diagram

We repeated the above procedure for a data cube of the boxed region during 07:45–08:45 UT masked with a running time window that has a full width half maximum (FWHM) of 10 minutes with cosine bell tapering on both sides. We shifted the window by 1 min at a time (only 6 such windows are independent in the 1 hr duration) and obtained a corresponding  $k$ - $\omega$  diagram, as shown in Figures 4(c)–(f) and Animation 4. The early  $k$ - $\omega$  diagrams are dominated by a shallow ridge with an increasing slope that indicates the CME acceleration. When the CME front moves out of the FOV, a steep ridge corresponding to the fast propagating waves becomes progressively evident with a slope varying in the  $1000$ – $2000 \text{ km s}^{-1}$  range.

### 2.2.3. Frequency Distribution of Fourier Power

We note that running difference (time derivative) in images used above, similar to a highpass filter, essentially scales the original signal with frequency  $\nu$  and applies a  $\nu^2$  factor to the Fourier power. To recover the intrinsic power amplitude, we replaced running difference images with detrended images obtained by subtracting images running-smoothed in time with a 200 s boxcar, introducing a low-frequency cutoff of 5 mHz that is below all strong peaks on the ridge in Figure 4(b). We

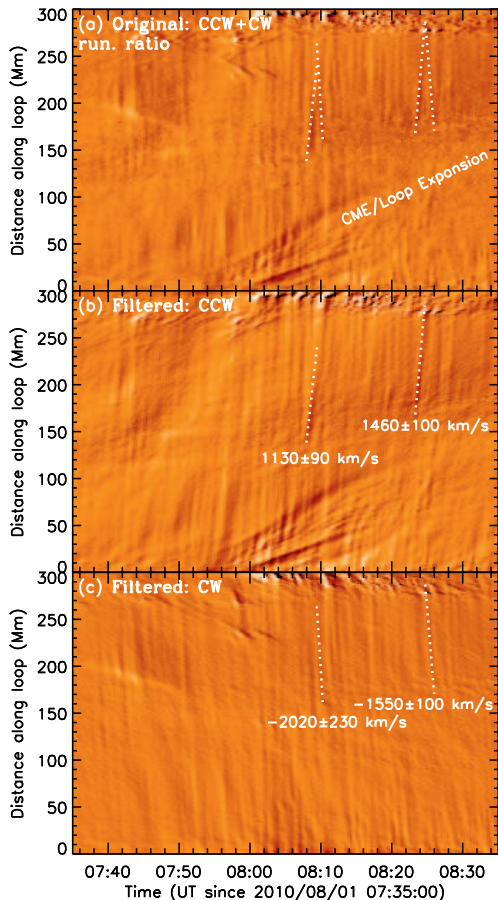


FIG. 3.— (a) AIA 171 Å running ratio space-time diagram from the curved cut along coronal loops shown in Figure 1(a). Distance is measured from the eastern footpoint. Note fast waves propagating in both counter-clockwise (CCW) and clockwise (CW) directions along the loop. (b) and (c) Fourier filtered version of (a) showing CCW and CW waves separately. The linear fits here are repeated in (a).

then repeated the above analysis in Sections 2.2.1 and 2.2.2. The new  $k$ - $\omega$  diagrams (e.g., Figure 4(g) vs. (e)) exhibit the expected general trend of decreasing power with frequency, and as a result the steep ridge becomes less evident at high frequencies.

We averaged the new version (not shown) of the overall  $k$ - $\omega$  diagram of Figure 4(b) in wave number and obtained a power spectrum for the QFP waves (Figure 4(h)). We repeated this for the new  $k$ - $\omega$  diagrams at different times (e.g., Figure 4(g)) and compiled a running spectrogram (Figure 4(i)). The waves display a broad frequency distribution (cf., Tomczyk et al. 2007), with power peaks of ratio 1:  $1/4.6 : 1/15.8$  ( $\propto \nu^{-1.8 \pm 0.2}$ ) at frequencies  $\nu = 5.5 \pm 0.4$ ,  $14.5 \pm 0.7$ , and  $25.1 \pm 0.7$  mHz of ratio 1 :  $(2.6 \pm 0.2) : (4.5 \pm 0.3)$ . For comparison, a triangle wave of  $\nu_0 = 5.5$  mHz has non-zero Fourier power (blue asterisks, Figure 4(h)) at frequencies of similar ratio 1 : 3 : 5 that drops faster with  $\nu^{-4}$ .

The Fourier power from running difference and detrended images yields consistent peak frequencies, which can be visually identified in the space-time domain. The lowest frequency  $\nu_0 = 5.5$  mHz ( $P_0 = 181 \pm 13$  s  $\approx 3$  min) manifests as slow modulations in Figures 2(b) and (d) at 08:06–08:18 UT. The next period  $69 \pm 3$  s (14.5 mHz), dominating the power from running difference images

(Figure 4(b)), matches the temporal spacing between bright stripes near 08:08 UT in Figures 2(a)–(c) and the period given by the sinusoidal fits (Figure 2(e)). The corresponding wave fronts are prominent in the original and Fourier filtered images (Figures 1(d)–(i), Animation 1(E)). These two periods are also evident in the emission profiles of Figure 2(f). The higher frequency 25.1 mHz ( $40 \pm 1$  s) has considerably weaker power and a close frequency of 23 mHz (see Figure 4(d)) can be seen in the spacing of narrow stripes near 08:01 UT (Figure 2(a)), when the other two frequencies are not yet strong.

### 2.3. Common 3 min Periodicity in Waves and Flare

As shown in Figure 5(b), the *RHESSI* X-ray flux and AIA 1600 Å fluxes of flare ribbons (particularly the brightest one in box 1 where the funnel is rooted, see Figure 1(b) and Animation 1(B)) exhibit bursty bumps at a 3 min period (5.5 mHz). The onsets of these pulsations (vertical dotted lines) coincide with those of the slow modulations on the QFP waves (Figure 5(a)). This can be also seen in the wavelet power of these flare emissions (Figures 5(d)–(g)). The Fourier power of the X-ray flux (green curve, Figure 4(h)) is consistent with that of the QFP waves  $\lesssim 10$  mHz, but significantly lower at higher frequencies. It also matches that of the triangle wave up to the third harmonics because of its triangular pulse shape (Figure 5(c)). In contrast, the 1600 Å flux of a background plage (box 3 in Figure 1(b)) is constantly dominated by the 5 min (3.5 mHz) photospheric p-mode oscillations (Figure 5(b) and (f)).

### 2.4. Estimate of Wave Energy and Magnetic Field

The energy flux carried by the QFP waves can be estimated with the kinetic energy of the perturbed plasma,  $E = \rho(\delta v)^2 v_{\text{ph}}/2 \geq \rho(\delta I/I)^2 v_{\text{ph}}^3/8$  (Aschwanden 2004), where we have assumed that the observed intensity variation  $\delta I$  results from density modulation  $\delta \rho$  and used  $\delta v/v_{\text{ph}} \geq \delta \rho/\rho = \delta I/(2I)$  for magnetosonic waves since  $I \propto \rho^2$ . If we take  $v_{\text{ph}} = 1600$  km s $^{-1}$  and  $\delta I/I = 1\%$ – $5\%$  observed in the mid-range of the funnel (200 Mm from the flare kernel), and use the corresponding number density  $n_e \gtrsim 10^8$  cm $^{-3}$  estimated with the 171 Å channel response (following De Pontieu et al. 2011), we reach an energy flux  $E \gtrsim (0.1\text{--}2.6) \times 10^5$  ergs cm $^{-2}$  s $^{-1}$ . The diameter of the funnel here has increased  $\sim 10$  times from the coronal base, where the wave energy flux shall be  $\gtrsim 10^2$  times higher by continuity of energy flow, if we assume the waves being generated there and consider damping on their path. This energy flux is more than sufficient for heating the *local* active region loops (Withbroe & Noyes 1977). However, considering the limited temporal and spatial extent of these waves, they are unlikely to play an important role in heating the quiescent *global* corona.

Assuming the measured phase speed  $v_{\text{ph}}$  equal to the fast mode speed along magnetic field lines in the funnel, which is the Alfvén speed  $v_A = B/\sqrt{4\pi\rho}$ , the magnetic field strength is estimated as  $B = v_{\text{ph}}\sqrt{4\pi\rho} \gtrsim 8$  G.

## 3. DISCUSSION

We propose that these QFP waves imaged with AIA’s unprecedented capabilities are fast mode magnetosonic



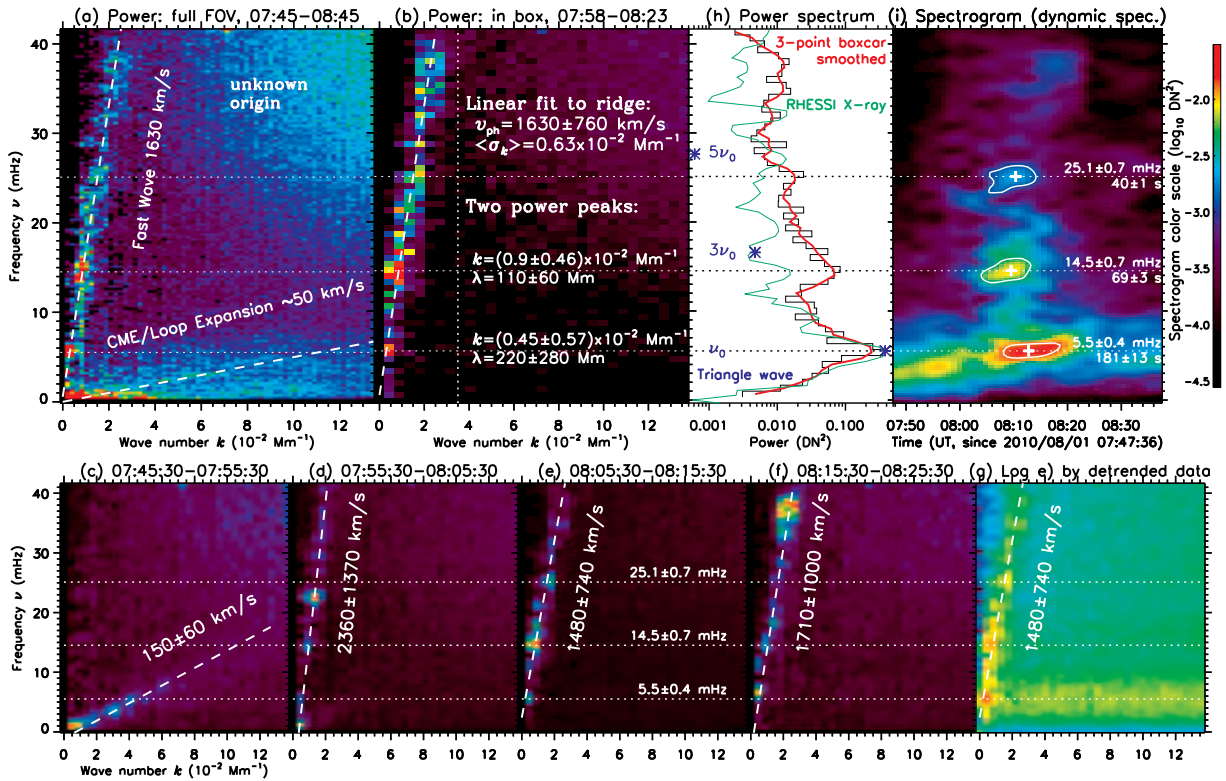


FIG. 4.— Fourier analysis of wave properties. (a) Fourier power ( $k$ - $\omega$  diagram) of a 3D data cube of 171 Å running difference images during 07:45–08:45 UT in the full FOV of Figure 1(a). (b) Same as (a) but for 07:58–08:23 UT in the boxed region of Figure 1(d). The white dashed line (repeated in (a)) is a power-weighted linear fit to the ( $k$ ,  $\nu$ ) positions of pixels greater than 10% of the maximum power in the  $k \leq k_{\max}$  range (marked by the vertical dotted line). (c)–(f) Same as (b) but for images masked with a running time window whose FWHM is labeled on each panel (see Animation 4). (g) Same as (e) but on log scale from detrended (rather than running difference) images (see Section 2.2.3). The diffuse horizontal band is an artifact at the 5 mHz detrending cutoff frequency and is  $\sim 5\%$  of the QFP wave power here. (h) Power spectrum vs. frequency obtained by averaging in  $k \leq k_{\max}$  on a  $k$ - $\omega$  diagram that is the same as (b) but from detrended images. (i) Spectrogram obtained by compiling wave number averaged power as shown in (h) from  $k$ - $\omega$  diagrams at different times as shown in (g). The x-axis here refers to central times of the running window. Prominent “islands” are contoured at the 50% level; their peaks are marked by plus signs and the peak frequencies (periods) by horizontal dotted lines. The frequency uncertainties are the standard deviations within the contours.

waves that have been theoretically predicted and simulated (e.g., Bogdan et al. 2003; Fedun et al. 2011; Ofman et al. in preparation), but rarely observationally detected. We speculate their possible origin as follows.

1. The accompanying CME is unlikely to be the wave trigger, because it takes place gradually for  $\sim 30$  min ( $\gg$  wave periods, Figure 2(b)) and its single pulse would be difficult to sustain oscillations lasting  $\sim 1$  hr as observed here without being damped. However, the environment in its wake might be favorable for these waves.
2. The common 3 min periodicity (Section 2.3) of the QFP waves and flare quasi-periodic pulsations (QPPs; Nakariakov & Melnikov 2009; Kupriyanova et al. 2010) suggests a common origin. Quasi-periodic magnetic reconnection and energy release can excite both flare pulsations (Ofman & Sui 2006; Fleishman et al. 2008) and MHD oscillations that drive QFP waves, or in turn, MHD oscillations responsible for the waves

can modulate energy release and flare emission (Foullon et al. 2005). This periodicity is the same as that of 3 min chromospheric oscillations, further suggesting their possible modulation on reconnection (Chen & Priest 2006; Heggland et al. 2009; McLaughlin et al. 2009).

However, the deficit of flare power at higher wave frequencies ( $\gtrsim 10$  mHz, Figure 4(h)) is somewhat puzzling. Perhaps the waves are driven by a multi-periodic exciter that produces no detectable flare signals at these frequencies. A future study of similar events will further shed light on the nature of these waves.

This work was supported by AIA contract NNG04EA00C. LO was supported by NASA grants NNX08AV88G and NNX09AG10G. Wavelet software was provided by C. Torrence and G. Compo. We thank Nariaki Nitta for helpful discussions.

#### REFERENCES

- Aschwanden, M. J. 2004, in ESA Special Publication, Vol. 575, SOHO 15 Coronal Heating, ed. R. W. Walsh, J. Ireland, D. Danesy, & B. Fleck, 97
- Aschwanden, M. J., Fletcher, L., Schrijver, C. J., & Alexander, D. 1999, *ApJ*, 520, 880
- Bogdan, T. J. et al. 2003, *ApJ*, 599, 626

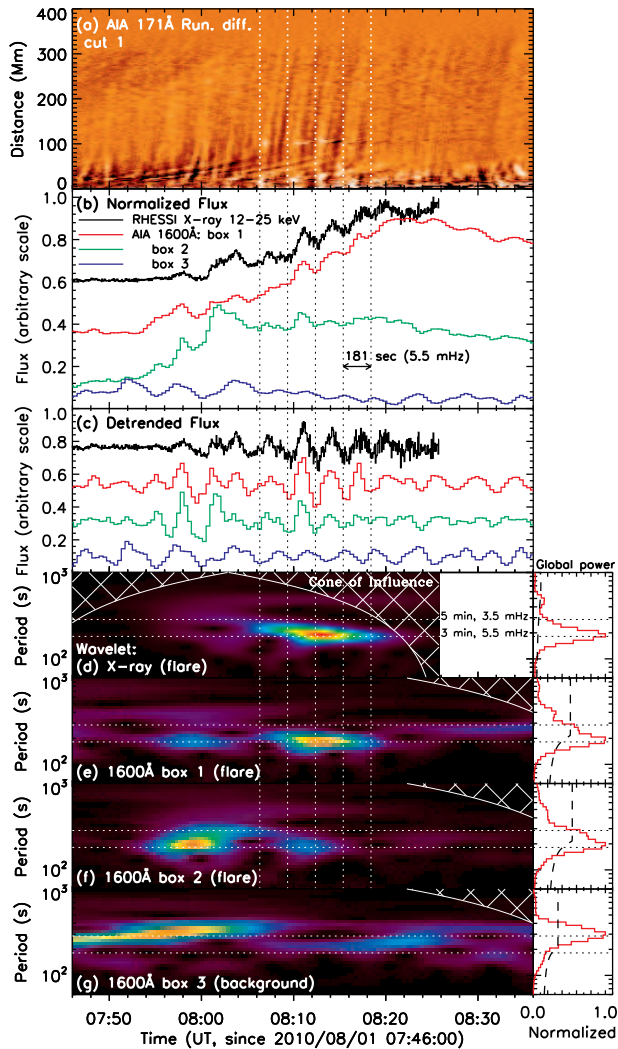


FIG. 5.— Quasi-periodic flare pulsations. (a) Same as Figure 2(a) but smoothed with a  $3 \times 3$  boxcar. (b) *RHESSI* 12-25 keV X-ray flux and AIA 1600 Å fluxes integrated over the boxes shown in Figure 1(b). (c) Same as (b) but for detrended fluxes obtained by subtracting smoothed fluxes using a 200 s boxcar. (d)–(g) Wavelet and global power of the curves in (c), but for extended durations to reduce the hatched cone of influence of edge effects (Torrence & Compo 1998). The dashed line in the global power indicates the 95% significance level. The horizontal dotted lines mark the 3.5 and 5.5 mHz frequencies (periods:  $\sim 5$  and 3 min). The vertical dotted lines mark the onsets of the 181 s modulations shown in Figure 2(f).

Chen, P. F. & Priest, E. R. 2006, *Sol. Phys.*, 238, 313  
 Chen, P. F. & Wu, Y. 2011, *ApJ*, 732, L20  
 Certain, J. W., et al. 2007, *Science*, 318, 1580

De Moortel, I., Ireland, J., & Walsh, R. W. 2000, *A&A*, 355, L23  
 De Pontieu, B., et al. 2011, *Science*, 331, 55  
 De Pontieu, B., et al. 2007, *Science*, 318, 1574  
 DeForest, C. E. 2004, *ApJ*, 617, L89  
 DeForest, C. E. & Gurman, J. B. 1998, *ApJ*, 501, L217  
 Fedun, V., Shelyag, S., & Erdélyi, R. 2011, *ApJ*, 727, 17  
 Fleishman, G. D., Bastian, T. S., & Gary, D. E. 2008, *ApJ*, 684, 1433  
 Foullon, C., Verwichte, E., Nakariakov, V. M., & Fletcher, L. 2005, *A&A*, 440, L59  
 Heggland, L., De Pontieu, B., & Hansteen, V. H. 2009, *ApJ*, 702, 1  
 Jess, D. B., Mathioudakis, M., Erdélyi, R., Crockett, P. J., Keenan, F. P., & Christian, D. J. 2009, *Science*, 323, 1582  
 Kupriyanova, E. G., Melnikov, V. F., Nakariakov, V. M., & Shibasaki, K. 2010, *Sol. Phys.*, 267, 329  
 Lemen, J. et al. 2011, accepted by *Sol. Phys.*  
 Liu, R., Liu, C., Wang, S., Deng, N., & Wang, H. 2010a, *ApJ*, 725, L84  
 Liu, W., Berger, T. E., Title, A. M., & Tarbell, T. D. 2009, *ApJ*, 707, L37  
 Liu, W., Nitta, N. V., Schrijver, C. J., Title, A. M., & Tarbell, T. D. 2010b, *ApJ*, 723, L53  
 McLaughlin, J. A., De Moortel, I., Hood, A. W., & Brady, C. S. 2009, *A&A*, 493, 227  
 Moreton, G. E. 1960, *AJ*, 65, 494  
 Nakariakov, V. M. & Melnikov, V. F. 2009, *Space Sci. Rev.*, 149, 119  
 Nakariakov, V. M., Melnikov, V. F., & Reznikova, V. E. 2003, *A&A*, 412, L7  
 Nakariakov, V. M. & Verwichte, E. 2005, *Living Reviews in Solar Physics*, 2, 3  
 Ofman, L., Romoli, M., Poletto, G., Noci, G., & Kohl, J. L. 1997, *ApJ*, 491, L111  
 Ofman, L. & Sui, L. 2006, *ApJ*, 644, L149  
 Ofman, L. & Thompson, B. J. 2002, *ApJ*, 574, 440  
 Ofman, L. & Wang, T. 2002, *ApJ*, 580, L85  
 Ofman, L. & Wang, T. J. 2008, *A&A*, 482, L9  
 Okamoto, T. J., et al. *Science*, 318, 1577  
 Schrijver, C. J. & Title, A. M. 2011, *J. Geophys. Res.*, in press  
 Schrijver, C. J., et al. 1999, *Sol. Phys.*, 187, 261  
 Thompson, B. J., Plunkett, S. P., Gurman, J. B., Newmark, J. S., St. Cyr, O. C., & Michels, D. J. 1998, *Geophys. Res. Lett.*, 25, 2465  
 Tomczyk, S. & McIntosh, S. W. 2009, *ApJ*, 697, 1384  
 Tomczyk, S., McIntosh, S. W., Keil, S. L., Judge, P. G., Schad, T., Seeley, D. H., & Edmondson, J. 2007, *Science*, 317, 1192  
 Torrence, C. & Compo, G. P. 1998, *Bulletin of the American Meteorological Society*, 79, 61  
 Van Doorselaere, T., Nakariakov, V. M., & Verwichte, E. 2008, *ApJ*, 676, L73  
 Verwichte, E., Nakariakov, V. M., & Cooper, F. C. 2005, *A&A*, 430, L65  
 Wang, T., Solanki, S. K., Curdt, W., Innes, D. E., & Dammasch, I. E. 2002, *ApJ*, 574, L101  
 Williams, D. R., Mathioudakis, M., Gallagher, P. T., Phillips, K. J. H., McAteer, R. T. J., Keenan, F. P., Rudawy, P., & Katsiyannis, A. C. 2002, *MNRAS*, 336, 747  
 Withbroe, G. L. & Noyes, R. W. 1977, *ARA&A*, 15, 363  
 Wu, S. T., Zheng, H., Wang, S., Thompson, B. J., Plunkett, S. P., Zhao, X. P., & Dryer, M. 2001, *J. Geophys. Res.*, 106, 25089